Contents lists available at ScienceDirect

International Journal of Heat and Mass Transfer

journal homepage: www.elsevier.com/locate/hmt



Hot-spot thermal management by phase change materials enhanced by spatially graded metal meshes



Lien Chin Wei^a, Ionathan A. Malen^{a,b,*}

- ^a Department of Mechanical Engineering, Carnegie Mellon University, Pittsburgh, PA 15213, USA
- ^b Department of Materials Science and Engineering, Carnegie Mellon University, Pittsburgh, PA 15213, USA

ARTICLE INFO

Article history:
Received 5 September 2019
Revised 19 November 2019
Accepted 30 November 2019
Available online 15 January 2020

Keywords:
Thermal management
Stefan problem
Thermal conductivity
Phase change material
Additive manufacturing
Latent heat

ABSTRACT

Graded mesh inserts that spatially enhance the thermal conductivity of phase change materials (PCM) are optimized to minimize the time averaged thermal resistance between the heat source and the meltfront, to improve heat dissipation rates for electronics. Conventionally, the low thermal conductivities of PCM are enhanced by incorporating spatially-homogeneous porous fillers with high thermal conductivities. We investigate the relative advantages of porous fillers that spatially distribute enhancements to thermal conductivity. An arbitrary polynomial form of the spatial variation is optimized based on a numerical solution to the heat diffusion equation, to enhance heat dissipation rates in one-dimensional spherical and cylindrical coordinates. The most desirable spatial distributions are non-linear, have higher thermal conductivity near to the hot-spot, and a positive second derivative with respect to the radial coordinate (i.e. concave-up). We demonstrate enhancements of heat dissipation rates for constant temperature hot-spots, or reductions in temperature for constant power hot-spots, by factors of 900% and 300% in spherical and cylindrical coordinates, relative to those achieved by uniform fillers of equivalent average volume fractions. Recent advances in additive manufacturing make metal meshes with spatially graded volume fraction realizable.

© 2019 Elsevier Ltd. All rights reserved.

1. Introduction

Improved computational performance of electronic devices, such as laptop computers and cellular telephones, demands more power while their size continues to shrink [3–6]. The result is increased volumetric heat generation rates, which challenge conventional thermal management strategies [3,4,7]. Active (e.g., fanblown air, thermoelectric coolers) and passive (e.g., heat sinks, heat pipes) cooling techniques have been widely investigated [4,8–10].

Passive thermal management consumes less power and is more reliable than active thermal management with fans and pumps [3]. Therefore, for small devices such as cellular telephones and tablets, passive thermal management is more desirable. Nevertheless, passive thermal management has limitations. For instance, gravity-driven heat pipes operate best when the device is in specific configurations, and passive heat sinks rely on natural convection with low heat transfer coefficients.

Phase change materials (PCM) that operate passively and absorb transient spikes in the heat load by the latent heat of the

phase change process are attractive alternatives to heat pipes and heat sinks. The transient temperature rise is affected by the composition of the PCM, the configuration of the thermal management systems, and the size and heat load of the hot-spots [3,7,11]. PCM, such as octadecane and eicosane, are commonly selected due to their phase change temperatures (30 °C to 40 °C), which maintain a comfortable device temperature for the users [3,7]. Nevertheless, due to the low thermal conductivity of such PCM, the thermal resistance of getting heat from the hot-spot to the melt-front is a major limitation to the heat dissipation rate. As a result heat from hot-spots may diffuse through unintended pathways instead of directly into PCM. To mitigate this effect, heat sinks have been embedded into PCM to minimize thermal resistance [11,12]. The drawback is that these embedded parts displace the latent heat benefit of PCM and add substantial weight to smaller devices.

An alternative approach to increase heat dissipation rates of PCM is through the addition of low volume fraction, high thermal conductivity, porous materials. The effective thermal conductivity of PCM can be enhanced by incorporating either dispersed fillers [13–18] or high thermal conductivity porous structures (e.g., metal foams or meshes) [18–22]. Because both fillers and porous structures are spatially homogeneous, the thermal conductivity of the PCM is uniformly-enhanced (UE).

^{*} Corresponding author.

E-mail address: jonmalen@andrew.cmu.edu (J.A. Malen).

Nomenclature $\bar{\nu}$ average volume fraction thermal conductivity difference (W m⁻¹ K⁻¹) Δk Δr $r_0 - r_i$ (m) ΔT temperature difference (K) C_i

adjustable coefficient of ith degree in Eq. (3)

 C_{p} fluid specific heat (J $kg^{-1} K^{-1}$) the acceleration of gravity (m s^{-2}) g k thermal conductivity (W m^{-1} K⁻¹)

L length (m)

the degree of the polynomial in Eq. (3) n constant heat source power (W) q r position in spherical coordinates (m) r

ratio of radii, r_0/r_1 R_{max} R_{\min} $R_{\min} = R_{\max} - 1$

inner radius of the spherical system (m) $r_{\rm i}$

melting front radial position in spherical coordi $r_{
m m}$

nates (m)

outer radius of the spherical system (m) r_{o}

Ra Rayleigh number Ste Stefan number Τ temperature (K) t time (s)

 T_{i} temperature at the inner sphere (K) T_{o} temperature at the outer sphere (K)

ν volume fraction

Greek Symbols

 α thermal diffusivity ($m^2 s^{-1}$)

fluid thermal expansion coefficient (K⁻¹) β $\Delta \kappa$ dimensionless thermal conductivity difference

dimensionless radial position step $\Delta \rho$

 $\Delta \tau$ dimensionless time step

dimensionless thermal conductivity К volumetric latent heat of fusion (J m⁻³) λ

 λ' latent heat of fusion (J kg⁻¹)

fluid viscosity (Pa s) μ

 $\Delta\theta$ dimensionless temperature difference

enhancement ratio of SE to UE PCM composites ϵ dimensionless radial position in cylindrical coordiρ nates

fluid density (kg m⁻³) ρ_{f}

dimensionless melting front position in spherical $ho_{
m sp,m}$

coordinates

dimensionless radial position in spherical coordi $ho_{
m sp}$

dimensionless time τ dimensionless temperature

Subscripts

ch characteristic C conduction

conservation of volume fraction cv

int integration melting front m maximum max Mesh metal mesh min minimum

PCM phase change material 1-D cylindrical coordinates r

S surface

SE spatial enhancement 1-D spherical coordinates sp UE uniform enhancement

Recent advancements in additive manufacturing (AM) provide a feasible way to fabricate complex metal architectures, such as graded lattices and meshes. By inserting graded meshes into PCM, the metal volume fraction can be spatially-varied, and thus the thermal conductivity becomes spatially-enhanced (SE) [23–26]. Such meshes make it possible to concentrate the enhancement near to the heat source, thus minimizing the thermal resistance for heat to reach the melt front [26]. For equivalent average volume fractions of mesh, a linear spatial variation can improve the heat dissipation rates by 12% in planar and 140% in cylindrical configurations [26]. Spatially-enhanced diffusivities with other mathematical forms, such as power law functions, have been studied for mathematically similar sedimentary mass transport applications [26-33], but not thermal management.

While prior studies focused on linear and cylindrical geometries, none have considered spatially-heterogeneous thermal conductivity on moving boundary problems in spherical geometries. To improve upon state of the art PCM based thermal management designs, we herein utilize a generalized polynomial function to determine the optimal radial thermal conductivity distributions in spherical and cylindrical PCM/mesh systems.

2. Methodology

2.1. The Stefan problem in spherical coordinates

A Stefan problem, defined by a phase change process with a moving melt-front, can be solved using the quasi-steady state approximation when the Stefan number Ste < 0.1 [26,31]. A small Stefan number indicates that the sensible heat is small compared to the latent heat and a steady state temperature distribution accurately describes the liquid region [31]. Melting in porous media is a complex process and thus there are additional limitations to our analysis [34-37]. Initially, the heat transfer mechanism is governed by conduction alone but it eventually transitions to a mixed regime of conduction and natural convection driven by buoyancy of the heated liquid nearest to the source. Our analysis considers the conduction only regime where the transition to natural convection is specified by a characteristic timescale [35] that has been estimated by Krishnan et al. [37]. For spherical systems [35,38] with a specified hot-spot size, we have identified the maximum outer radius of the PCM for several hot-spot temperatures (in Appendix A). For example, a hot-spot with 100 µm radius elevated by 10 K will be conduction dominated for the entire melt process when the surrounding PCM sphere has a radius smaller than 5 mm. Our analysis also assumes local thermal equilibrium between the solid mesh and the PCM. Local thermal equilibrium can be sought for a given ratio of mesh and PCM thermal conductivities by varying and characteristic lengthscales of the mesh struts and unit cell volumes [39-42].

Hot-spots drive radial temperature gradients in the surrounding media, and thus the radial direction is considered in the spherical heat diffusion equation [43] (a parallel derivation for cylindrical coordinates can be found in Appendix E). The heat diffusion equation under the quasi-steady state approximation with temperature independent properties in a one dimensional spherical system is

$$\frac{1}{r^2} \frac{\partial}{\partial r} \left[r^2 k(r) \frac{\partial T(r,t)}{\partial r} \right] = 0, \tag{1}$$

where r is the radial coordinate, k(r) is the spatially-varied thermal conductivity of a PCM/mesh composite, T(r, t) is the temperature of the composite, and t is time. Schematics of PCM/Mesh composites with spatially-enhanced thermal conductivity k(r) are shown in Fig. 1. The hot-spot at a temperature $T(r_i, t) = T_s$ is surrounded by a spherical PCM/Mesh shell with inner and outer radii r_i and r_0 .

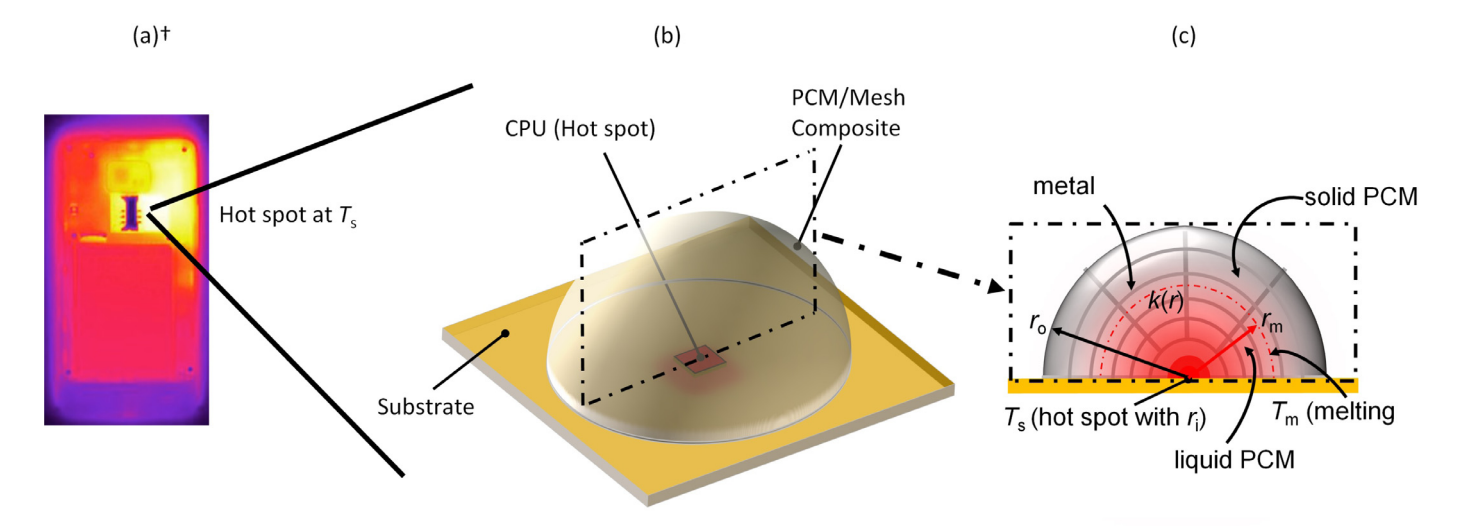


Fig. 1. Schematic of a hemi-spherical PCM/Mesh composite for thermal management. For the hot-spot to be seen clearly, the mesh structure is only shown in the cross-section view. (a) An infrared image of a mobile phone micro processor (i.e., chip †Ref. [1]) shows a localized hot-spot (e.g., hot-spots in Si microprocessors can be hundreds of microns in size [2]). (b) The heat generated at the hot-spot is absorbed by the phase change process in the PCM/Mesh composite. (c) The cross-sectional view of the hemi-spherical PCM/Mesh composite depicts a spatial variation in volume fraction of metal mesh, which results in spatially-enhanced thermal conductivity k(r).

The time dependent position of the melt-front relative to the hotspot (or heat source) is $r_{\rm m}(t)$, and the temperature at this position is the melting temperature $T(r_{\rm m}(t),t)=T_{\rm m}$.

Typical heat sources can be approximated with either constant heat flux, or constant temperature boundary conditions at $r=r_{\rm i}$. Spatial enhancement of thermal conductivity can similarly improve performance in both cases. For the constant temperature boundary condition spatial enhancement of thermal conductivity increases the heat transfer rate, while for the constant heat flux boundary condition spatial enhancements of thermal conductivity reduce the temporally averaged temperature of the heat source (see the detailed derivation in Appendix F). Parallel heat spreading in the chip will influence the hot spot size and temperature but has not been considered here. The following analysis focuses on the constant temperature condition but enhancement factors referring to increased heat transfer rate, can be interpreted as reduced temperature in the condition of constant heat flux.

With constant temperature boundary conditions of $T(r_i,t) = T_s$ and $T(r_m(t),t) = T_m$, the temperature of the composite for $r_i < r < r_m(t)$ can be determined. The temperature in the solid PCM beyond $r_m(t)$ (for a melt process) is assumed to be at T_m , so no additional sensible heat is required [26,31].

The energy balance at the melt-front is

$$-k(r)\frac{\partial T(r,t)}{\partial r}\Big|_{r=r_{\rm m}(t)} = \lambda \frac{dr_{\rm m}(t)}{dt}.$$
 (2)

For small mesh volume fractions the latent heat of fusion λ is assumed to be independent of r [26].

Our analysis of the spatially enhanced PCM is nondimensionalized to the uniformly-enhanced PCM. Upon nondimensionalizing the coordinate $\rho_{\rm sp}=(r-r_{\rm i})/(r_{\rm o}-r_{\rm i})$, the dimensionless thermal conductivity is defined as $\kappa(\rho_{\rm sp})=k(\rho_{\rm sp})/k_{\rm UE}$ and formulated as a polynomial

$$\kappa(\rho_{sp}) = C_n \rho_{sp}^{\ n} + C_{n-1} \rho_{sp}^{\ n-1} + \dots + C_1 \rho_{sp} + C_0$$

$$= \sum_{i=0}^{i=n} C_i \rho_{sp}^{\ i},$$
(3)

where C_i are the adjustable coefficients of the ith degree terms that will be optimized, and n is the degree of the polynomial. Although mathematical forms of dimensionless thermal diffusivity or thermal conductivity, such as power law and linear func-

tions, were previously introduced [26–28,30,33], this polynomial form adds degrees of freedom to generate more complex spatial-variations of thermal conductivity.

2.2. Nondimensionalized solution for a spatially-enhanced thermal conductivity in 1-D spherical coordinates

We nondimensionalize Eq. (1) by substitution of $\rho_{\rm sp}$, $\kappa(\rho_{\rm sp})$, the ratio of bounding radii $R_{\rm max}=r_{\rm o}/r_{\rm i}$, and dimensionless temperature $\theta(\rho_{\rm sp},\tau_{\rm sp})=\left[T\left(\rho_{\rm sp},\tau_{\rm sp}\right)-T_{\rm m}\right]/(T_{\rm s}-T_{\rm m})$. The dimensionless time $\tau_{\rm sp}=t/t_{\rm sp,max}$ is defined based upon the time required to melt all of the PCM in the case of uniformly-enhanced thermal conductivity $t_{\rm sp,max}=\lambda r_{\rm i}^2(2R_{\rm max}^3-3R_{\rm max}^2+1)/[6k_{\rm UE}(T_{\rm s}-T_{\rm m})]$ (see Appendix B for the derivation of $t_{\rm sp,max}$). The resulting nondimensional radial heat diffusion equation is,

$$\frac{1}{(1+\rho_{\rm sp}R_{\rm min})^2}\frac{\partial}{\partial\rho_{\rm sp}}\left[(1+\rho_{\rm sp}R_{\rm min})^2\kappa(\rho_{\rm sp})\frac{\partial\theta(\rho_{\rm sp},\tau_{\rm sp})}{\partial\rho_{\rm sp}}\right]=0,$$
(4)

where $R_{\min} = R_{\max} - 1$.

The energy balance from Eq. (2) is nondimensionalized using the same parameters

$$-\kappa (\rho_{sp}) \frac{\partial \theta (\rho_{sp}, \tau_{sp})}{\partial \rho_{sp}} \Big|_{\rho_{sp} = \rho_{sp,m}(\tau_{sp})}$$

$$= \left(\frac{6R_{\min}^2}{2R_{\max}^3 - 3R_{\max}^2 + 1} \right) \frac{d\rho_{sp,m}(\tau_{sp})}{d\tau_{sp}}, \tag{5}$$

where $ho_{\rm sp,m}(\tau_{\rm sp})$ is the dimensionless melt-front position in spherical coordinates. As $R_{\rm max}\approx 1$, the term in parentheses of Eq. (5) approaches 2 and is the same as Eq. (6) from Ref. [26] for 1-D Cartesian coordinates, indicating that a thin spherical shell $(r_0-r_i\ll r_i)$ behaves like a planar solid.

An analytical solution to Eq. (4), after substitution of $\kappa(\rho_{sp})$ from Eq. (3), does not exist. Thus, $\rho_{sp,m}$ is numerically solved from Eqs. (4) and (5). Hereby the numerical model is solved using a 1-D, finite volume scheme, and an explicit (or forward) Euler method. The numerical details are in Appendix C. The maximum of $\rho_{sp,m}$ is 1, and $\tau_{sp,max} = \tau_{sp}(\rho_{sp,m} = 1)$. Because the same volume of PCM is melted, $\tau_{sp,max} < 1$ signifies that the SE thermal conductivity distribution dissipates heat faster than the UE thermal conductivity

Table 1 Properties and parameters used to determine $\kappa(\rho_{\rm sp})$.

PCM/Mesh	k _{PCM} (W/m-K)	k _{Mesh} (W/m-K)	$ar{v}_{Mesh}$	k _{UE} (W/m-K)	κ_{\min}	K _{max}
Octadecane/Al mesh	0.15 [44]	237 [43]	0.02	4.89	0.03	9.72

distribution. The reciprocal of $\tau_{\rm sp,max}$ is defined as the heat dissipation rate enhancement ratio of SE to UE PCM composites,

$$\epsilon_{\rm sp} = \frac{1}{\tau_{\rm sp,max}}.\tag{6}$$

In the case of the constant power hot-spot, the same $\epsilon_{\rm sp}$ would represent a reduced time averaged hot-spot temperature for SE relative to UE meshes.

2.3. Parameterization of thermal conductivity in a polynomial form

To constrain the form of $\kappa(\rho_{\rm Sp})$ constraints that equate the average volume fraction of metal mesh in UE and SE cases are now applied. The local volume fraction and thermal conductivity are related by an effective medium model. Because the metal mesh and PCM are bi-continuous phases, the Parallel Model is appropriate [26,45], and $k(\rho_{\rm Sp})=k_{\rm PCM}+\Delta k~\nu_{\rm Mesh}(\rho_{\rm Sp})$ where $k_{\rm PCM}$ is the thermal conductivity of the PCM, $\Delta k=k_{\rm Mesh}-k_{\rm PCM}$ is the thermal conductivity difference, $k_{\rm Mesh}$ is the thermal conductivity of the metal mesh, and $\nu_{\rm Mesh}$ is the volume fraction of the metal mesh. The dimensionless thermal conductivity ($\kappa(\rho_{\rm Sp})=k(\rho_{\rm Sp})/k_{\rm UE}$) is defined as

$$\kappa(\rho_{\rm sp}) = \frac{k_{\rm PCM} + \Delta k \ \nu_{\rm Mesh}(\rho_{\rm sp})}{k_{\rm UE}},\tag{7}$$

The average mesh volume fraction of the SE distribution, $\bar{\nu}_{\text{Mesh}} = \left[\int_{r_{\rm i}}^{r_{\rm o}} 4\pi \, r^2 \, \nu_{\text{Mesh}}(\rho_{\rm sp}) \, dr \right] / [4\pi \, (r_{\rm o}^3 - r_{\rm i}^3)/3]$, is equated to the volume fraction of the UE distribution $\nu_{\rm UE}$.

With this constrained $v_{\text{Mesh}}(\rho_{\text{sp}})$ the coefficients C_i that define $\kappa(\rho_{\text{sp}})$ from Eq. (3) are related as

$$\sum_{i=0}^{i=n} C_{cv,i} C_i = 1, \tag{8}$$

where $C_{\text{cv},i}$ (see the detailed derivation in Appendix D) take the form

$$C_{\text{cv},i} = \left[\frac{(R_{\text{max}} - 1)^2}{i + 3} + \frac{2(R_{\text{max}} - 1)}{i + 2} + \frac{1}{i + 1} \right] \frac{3(R_{\text{max}} - 1)}{R_{\text{max}}^3 - 1}.$$
 (9)

The coefficients C_i are also constrained such that $v_{\text{Mesh}}(\rho_{\text{sp}}) > 0$, because a volume fraction cannot be negative. When $v_{\text{Mesh}}(\rho_{\text{sp}}) = 0$ the dimensionless thermal conductivity at that position is $\kappa\left(\rho_{\text{sp}}\right) = k_{\text{PCM}}/k_{\text{UE}}$. As an upper limit $v_{\text{Mesh}}(\rho_{\text{sp}}) < 0.2$ are considered, for which the latent heat of the PCM/Mesh composite is typically reduced by less than 10% relative to the pure PCM [26].

3. Results and discussion

3.1. Parametric evaluation of the polynomial $\kappa(\rho_{sp})$ distribution

For planar and cylindrical geometries a linear thermal conductivity distribution, peaked at the heat source, enhances dissipation rates by reducing the time averaged thermal resistance between the heat source and the melt-front [26]. The effects of concavity and maxima/minima position are now considered for the spherical geometry with the more versatile polynomial distribution proposed in Eq. (3) (Table 2).

In Fig. 2, four representative combinations of $\kappa(\rho_{\rm sp})$ are shown with a polynomial of degree n=2 in Eq. (3) using properties and

Table 2 Coefficients C_i for the parabolic $\kappa(\rho_{\rm sp})$ profiles shown in Fig. 2.

R _{max}	Concave	C ₀	C ₁	C ₂
1.00001	down	1.48178	0.0	-1.44532
1.00001	up	2.9271	-5.7813	2.8907
101	down	2.42745	0.0	-2.39100
101	up	9.4821	-18.8914	9.4457

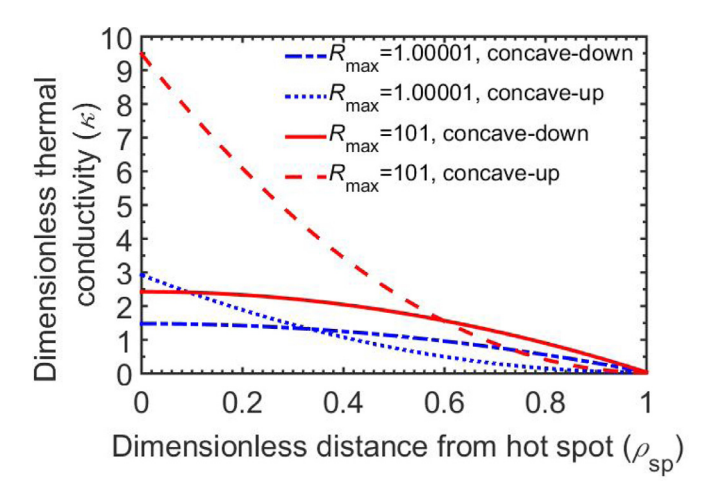


Fig. 2. The combinations of spatial variation of $\kappa(\rho_{\rm sp})$ of degree n=2 in Eq. (3) are constrained by the conservation of volume fraction and limitations on the minimum/maximum of $\kappa(\rho_{\rm sp})$ (i.e., $\kappa_{\rm min}$ and $\kappa_{\rm max}$) listed in Table 1. The concave-up $\kappa(\rho_{\rm sp})$ provides a higher thermal conductivity near the hot-spot.

parameters listed in Table 1. Near to the heat source ($\rho_{\rm sp} \approx 0$) the value of $\kappa(\rho_{\rm sp})$ with $R_{\rm max}=101$ is higher than $\kappa(\rho_{\rm sp})$ with $R_{\rm max}=1.00001$, because the high $v_{\rm Mesh}(0)$ is compensated by low $v_{\rm Mesh}(\rho_{\rm sp})$ of spherical shells at more distant radii.

For the same $R_{\rm max}$, Eq. (3) can generate parabolic $\kappa(\rho_{\rm sp})$ with both concave-up and concave-down shapes as shown in Fig. 2. The concave-up shapes have minima at $\rho_{\rm sp}=1$, while the concave-down shapes have maxima at $\rho_{\rm sp}=0$. To maximize κ near the heat source its minimum is chosen to be at $\rho_{\rm sp}=1$. For instance, with $R_{\rm max}=1.00001$ as shown in Fig. 2, the concave-up case ($\kappa(\rho_{\rm sp})\approx3$) is 100% higher than the concave-down case ($\kappa(\rho_{\rm sp})\approx1.5$) at $\rho_{\rm sp}=0$. The difference is even more extreme with $R_{\rm max}=101$ where the concave-up case ($\kappa(\rho_{\rm sp})\approx9.5$) is 280% higher than the concave-down case ($\kappa(\rho_{\rm sp})\approx2.5$) at $\rho_{\rm sp}=0$.

How does enhancing $\kappa(\rho_{sp})$ near the heat source change the heat dissipation rate for these polynomial distributions? Fig. 3 shows the dimensionless distance of the melt-front from the hotspot, as a function of time for $R_{max}=101$. Concave-up $\kappa(\rho_{sp})$ results in $\tau_{sp,max}=0.12$, which is more than eight times faster than UE ($\epsilon_{sp}=8.2$). By comparison, concave down results in $\tau_{sp,max}=0.41$, which is just less than two and a half times faster than UE ($\epsilon_{sp}=2.4$). This result confirms that higher enhancement at the heat source $\rho_{sp}=0$ expedites the melting process and thus enhances the heat dissipation rates of PCM in spherical systems as was shown previously in Cartesian and cylindrical systems from Ref. [26]. In the case of the constant heat flux boundary condition the same ϵ_{sp} would represent a reduced temporally averaged hotspot temperature.

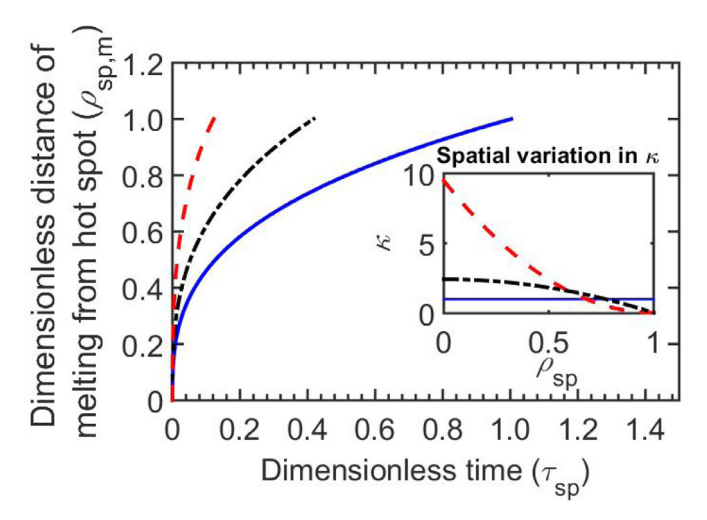


Fig. 3. The higher spatially-enhanced thermal conductivity near to the hot-spot (i.e., the intercept of $\kappa(\rho_{sp})$) with $R_{max}=101$ expedites the melting front ending at $\tau_{sp}=0.12$, and, in other words, increases the heat dissipation rate relative to UE by more than eight times.

3.2. Optimizing the concave-up distribution

Given the performance benefits of a concave-up $\kappa(\rho_{\rm sp})$, Eq. (3) is now specified so that $\kappa(\rho_{\rm sp})$ is always concave-up, as

$$\kappa(\rho_{\rm sp}) = \Delta\kappa (1 - \rho_{\rm sp})^n + \kappa_{\rm min},\tag{10}$$

where $\Delta \kappa$ is the dimensionless thermal conductivity difference between $\rho_{\rm sp}=0$ and $\rho_{\rm sp}=1$. With this definition $v_{\rm Mesh}$ is determined by equating Eqs. (7) and (10). The result, $v_{\rm Mesh}(\rho_{\rm sp})=\left[\Delta\kappa\left(1-\rho_{\rm sp}\right)^n+(\kappa_{\rm min}-k_{\rm PCM}/k_{\rm UE})\right]k_{\rm UE}/\Delta k$, is substituted into Eq. (D.1) to enforce volume fraction conservation. As a result, $\Delta\kappa$ is

$$\Delta \kappa = \frac{1 - \kappa_{\min}}{\frac{3(R_{\max} - 1)}{R_{\max}^2 - 1} \left[\frac{(R_{\max} - 1)^2}{n + 3} - \frac{2(R_{\max} - 1)R_{\max}}{n + 2} + \frac{R_{\max}^2}{n + 1} \right]}.$$
 (11)

For the uniformly-enhanced $\kappa(\rho_{\rm sp})$ where n=0 and $\Delta\kappa=1-\kappa_{\rm min}$, we recover $\kappa(\rho_{\rm sp})=1$ from Eq. (10).

Concave-up shapes are preserved by Eq. (10) even with n>2 because the second derivative of Eq. (10) is always positive for $0 \le \rho_{\rm sp} \le 1$. For the same $\kappa_{\rm min}$ in Eq. (10), higher order n result in larger $\Delta \kappa$ and thus higher intercepts of $\kappa(\rho_{\rm sp})$. Nevertheless, the highest $\kappa(\rho_{\rm sp})$ for each n is herein constrained by maintaining $v_{\rm Mesh}(\rho_{\rm sp}) < 0.2$, as not to replace too much PCM with mesh, per the discussion in Section 2.3.

There are significant gains by moving beyond simple linear distributions of thermal conductivity (i.e., n=1). The enhancement ratio using Eq. (10) is shown in Fig. 4 and indicates that heat dissipation rates are not further enhanced with n>3 for $R_{\rm max}=101$. This conclusion results due to the constraints on $\kappa_{\rm min}$ and $\kappa_{\rm max}$, which limit the utility of higher degree polynomials and may change if these constraints are adjusted.

3.3. Effects by ratio of radii

In Fig. 5 $\epsilon_{\rm sp}$ versus $R_{\rm max}$ is shown for spherical and cylindrical coordinates with n=1,2, and 3. The analysis with the polynomial $\kappa(\rho_{\rm sp})$ distribution for cylindrical systems is derived in Appendix E. Remarkably, in spherical systems the enhancement ratio with n=3 reaches 9.4 for $R_{\rm max}=1000$. For cylindrical systems with similar $R_{\rm max}$, the enhancement ratio is 3.2 for n=2 and 3.7 for n=3. For n=2 and 3, $\epsilon_{\rm sp}$ exceed that of n=1 for $R_{\rm max}>10$, which

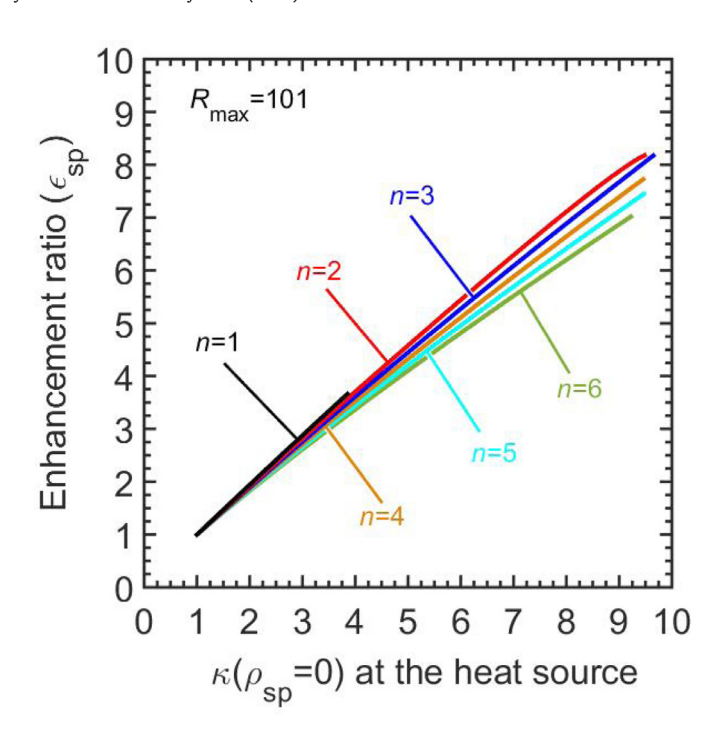


Fig. 4. The enhancement ratio using Eq. (10) indicates that complex concave-up $\kappa(\rho_{\rm sp})$ with degree higher than 1 (i.e., n>1) enhance heat dissipation rates by a factor of nearly 8.

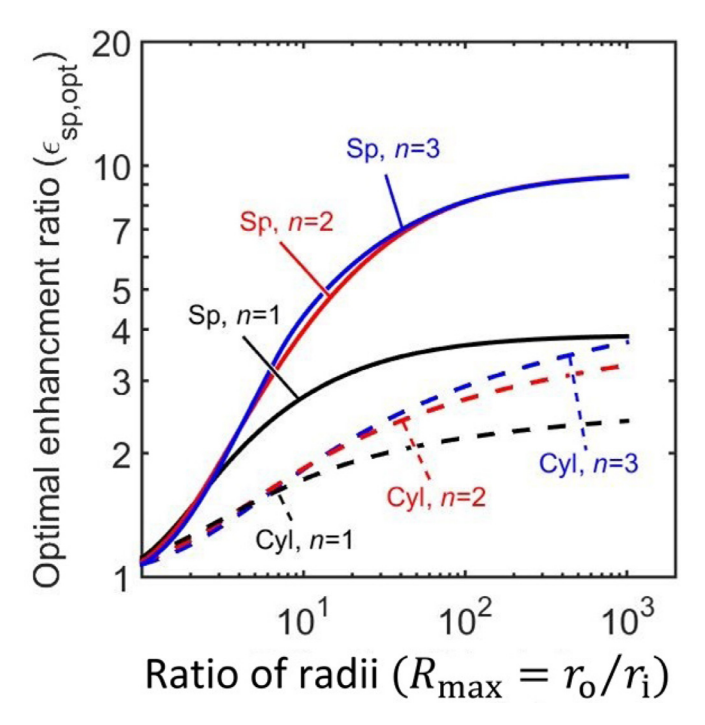


Fig. 5. The optimal enhancement ratio as a function of the ratio of radii in cylindrical (Cyl) and spherical (Sp) systems. The optimal enhancement ratio ($\epsilon_{\text{sp.opt}}$) reaches 9.4 for n=2 and n=3 in spherical systems with $R_{\text{max}}=1000$. For the cylindrical systems with similarly large R_{max} , the enhancement ratio ($\epsilon_{r,\text{opt}}$) is 3.2 for n=2 and 3.7 for n=3. In both cylindrical and spherical systems, the enhancement to thermal transport for higher order polynomials is distinctively better than for n=1 (i.e., spatially-linear $\kappa(\rho_{\text{sp}})$).

clearly demonstrates the value of using polynomial distributions of $\kappa(\rho_{\rm Sp})$. These extreme enhancements of the heat dissipation rates by factors of more than 900% and 300% in spherical and cylindrical coordinates will vastly benefit thermal management strategies, enabling higher powers or lower weights in portables.

More extreme enhancements can be achieved in spherical coordinates because in a homogeneous solid sphere the derivative of thermal resistance, which represents the thermal resistance per unit spherical shell thickness, is highest at $r=r_{\rm i}$ (i.e., thermal resistance accumulates most rapidly when the melt front is near $r=r_{\rm i}$). Mathematically, the derivatives of thermal resistance are proportional to $1/r^2$ and 1/r for spherical and cylindrical systems. When r is near to $r_{\rm i}$, the thermal resistance accumulates more rapidly for spherical than cylindrical geometries.

4. Conclusion

This study pioneers an arbitrary polynomial form of spatially-varied thermal conductivity to enhance heat dissipation rates in PCM for thermal management. Heat dissipation rates are enhanced using a concave-up thermal conductivity distribution that is highest near to the heat source in both 1-D spherical and 1-D cylindrical systems. While the results are derived in terms of enhancement to heat transfer rate for a constant temperature heat source, an equally valid interpretation is a reduction in the temporally averaged hot-spot temperature in the case of a constant heat flux source.

For spherical and cylindrical systems, the heat dissipation rates are enhanced by a factor of more than 900% and 300% relative to the uniformly enhanced case using spatially-parabolic thermal conductivity distributions.

For cylindrical systems, the enhancement ratio exceeds 300%. Practically these polynomial distributions could be used to vastly improve hot-spot thermal management with spatially enhanced meshes of equal weight or to create equivalent heat dissipation using SE meshes of significantly reduced weight.

Declaration of Competing Interest

Jonathan A Malen, Lien Chin Wei certify that they have no affiliations with or involvement in any organization or entity with any financial interest (such as honoraria; educational grants; participation in speakers bureaus; membership, employment, consultancies, stock ownership, or other equity interest; and expert testimony or patent-licensing arrangements), or non-financial interest (such as personal or professional relationships, affiliations, knowledge or beliefs) in the subject matter or materials discussed in this manuscript.

CRediT authorship contribution statement

Lien Chin Wei: Conceptualization, Formal analysis, Writing - original draft, Writing - review & editing. **Jonathan A. Malen:** Conceptualization, Writing - original draft, Writing - review & editing.

Acknowledgments

We acknowledge partial support from the National Science Foundation under award number CBET-1804752.

Appendix A. Length scale for a melting process dominated by heat conduction

References [34–37] identified a time scale $t_{\rm c}$ where heat conduction dominates, and here it is assumed that if $t_{\rm sp,max} < t_{\rm c}$, the conduction regime will be valid. The time scale [37], converted from a dimensionless time $\tau_{\rm c}$, takes the form

$$t_{\rm c} = \tau_{\rm c} \frac{L_{\rm ch}^2}{\alpha},\tag{A.1}$$

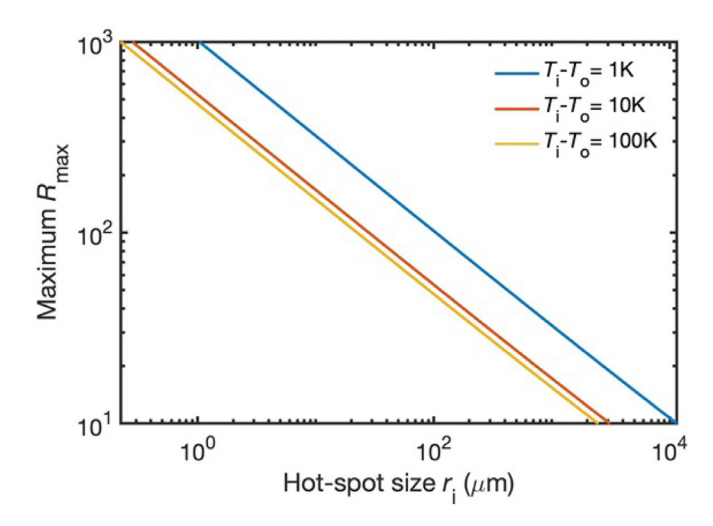


Fig. A.1. The maximum values of R_{max} where heat conduction regime is valid are estimated using various r_{i} temperature differences, $T_{\text{i}} - T_{\text{o}}$.

Table A.1 Properties and parameters used to determine length scales in Fig. A.1.

r _i (μm)	$10^{-1} - 10^4$				
$\Delta T = T_{\rm i} - T_{\rm o} (\rm K)$	1	10	100		
$k = k_{UE} \text{ (W/m-K)}$		4.89			
$\rho_{\rm f} ({\rm kg/m^3}) [46]$		763			
β (K ⁻¹) [47]	0.000764				
μ (Pa-s) [46]	0.002466				
$C_{\rm p}$ (J/kg-K) [48]	2140				
λ' (J/kg) [48]	210000				
$Ste = C_{\rm p} \Delta T / \lambda'$	0.01	0.1	1		

where $L_{\rm ch}$ is the characteristic length scale of the geometry, and α is the thermal diffusivity of the mesh/PCM matrix. For a concentric spherical enclosure, $L_{\rm ch}$ is the diameter of the inner sphere $(2r_{\rm i})$ [38]. The dimensionless time scale $\tau_{\rm c}$ in (A.1) dominated by heat conduction [37] is defined as

$$\tau_{c} = \frac{9Ra^{-\frac{1}{2}}}{Ste},\tag{A.2}$$

where Ste is the Stefan number and Ra is the Rayleigh number defined as

$$Ra = \frac{g\rho_{\rm f}\beta L_{\rm ch}^3(T_{\rm i}-T_{\rm o})}{\mu\alpha}, \tag{A.3}$$

where g is the acceleration of gravity, $\rho_{\rm f}$ is the fluid density, $T_{\rm i}$ is the temperature at the inner sphere, $T_{\rm o}$ is the temperature at the outer sphere, and β , μ , α are thermal expansion coefficient, viscosity, and thermal diffusivity.

By equating t_c with $t_{sp,max}$ (see Eq. (B.3) in Appendix B) we can determine the maximum value of R_{max} that maintains the conduction regime over the entire melting process for a given r_i . The maximum R_{max} , is plotted as a function of r_i , in Fig. A.1 for several $T_i - T_o$. Smaller hot-spot sizes and lower temperature gradients suppress natural convection and make the conduction-only analysis suitable to larger R_{max} .

Appendix B. Derivation of the maximum melting time $(t_{sp,max})$

The time for the melt-front to reach r_0 in 1-D spherical coordinates is $t_{\rm sp,max}$. The maximum melting time for uniform mesh ($k_{\rm UE}$) is determined when $k_{\rm UE}$ is substituted for k(r) in Eqs. (1) and (2). The temperature distribution is substituted into Eq. (2) as

$$k_{\rm UE} \left(\frac{T_{\rm s} - T_{\rm m}}{1/r_{\rm i} - 1/r_{\rm m}(t)} \right) \frac{1}{r^2} \bigg|_{r = r_{\rm m}(t)} = \lambda \frac{dr_{\rm m}(t)}{dt},$$
 (B.1)

and $t_{sp,max}$ is acquired by integration as

$$\int_{0}^{t_{\rm sp,max}} dt = \int_{r_{\rm i}}^{r_{\rm o}} dr_{\rm m}(t) \left(\frac{r_{\rm m}(t)^{2}}{r_{\rm i}} - r_{\rm m}(t) \right) \left[\frac{\lambda}{k_{\rm UE}(T_{\rm s} - T_{\rm m})} \right]. \quad (B.2)$$

The maximum melting time takes the form

$$t_{\text{sp,max}} = \frac{\lambda r_{\text{i}}^2 (2R_{\text{max}}^3 - 3R_{\text{max}}^2 + 1)}{6k_{\text{UE}}(T_{\text{s}} - T_{\text{m}})}$$
(B.3)

Appendix C. Derivation of the numerical solution in the dimensionless form

The normalized melt-front position $\rho_{\rm sp,m}$ is discretized as $\rho_{\rm sp,m,\it i}=(\it i-1)\Delta\rho_{\rm sp}$ where $\Delta\rho_{\rm sp}=1/N$ and the node index $\it i$ ranges from 1 to $\it N+1$. In this study, $\it N=1000$ was validated in comparison with the analytical solutions as shown in Fig. C.1 and thus is the default setting for the following analysis.

Since the discretized temporal melt-front is known to progress from $\rho_{\mathrm{sp},\mathrm{m},i=1}=0$ to $\rho_{\mathrm{sp},\mathrm{m},i=N+1}=1$, the cumulative melting time $\tau_{\mathrm{sp},i}=\tau_{\mathrm{sp},i-1}+\Delta\tau_{\mathrm{sp},i}$ is determined based on the associated time step $\Delta\tau_{\mathrm{sp},i}$ from node i-1 to node i.

After the first analytical integration, Eq. (4) becomes

$$(1 + \rho_{\rm sp} R_{\rm min})^2 \kappa (\rho_{\rm sp}) \frac{\partial \theta (\rho_{\rm sp}, \tau_{\rm sp})}{\partial \rho_{\rm sp}} = C_{{\rm int},i}, \tag{C.1}$$

where $C_{\mathrm{int},i}$ is the integration constant for node i. This integration constant is then acquired using numerical integration at each node as

$$C_{\text{int},i} = \frac{\int_{\theta(\rho_{\text{sp}} = \rho_{\text{sp,m,i}}, \tau_{\text{sp}}) = 0}^{\theta(\rho_{\text{sp}} = 0, \tau_{\text{sp}}) = 1} d\theta}{\int_{0}^{\rho_{\text{sp,m,i}}} \frac{d\rho_{\text{sp}}}{(1 + \rho_{\text{sp}} R_{\text{min}})^{2} \kappa(\rho_{\text{sp}})}}$$

$$= \frac{-1}{\int_{0}^{\rho_{\text{sp,m,i}}} \frac{d\rho_{\text{sp}}}{(1 + \rho_{\text{sp}} R_{\text{min}})^{2} \kappa(\rho_{\text{sp}})}}.$$
(C.2)

The time step $\Delta au_{\mathrm{sp},i=n}$ is then acquired by substituting $\kappa \left(
ho_{\mathrm{sp}} \right) \left[\partial \theta \left(
ho_{\mathrm{sp}}, au_{\mathrm{sp}} \right) / \partial \rho_{\mathrm{sp}} \right] = C_{\mathrm{int},i} / \left(1 + \rho_{\mathrm{sp}} R_{\mathrm{min}} \right)^2$ from Eq. (C.1) into the energy balance Eq. (5) and then discretizing to reach

$$\Delta \tau_{\mathrm{sp},i} \approx \left(\frac{6R_{\mathrm{min}}^2}{2R_{\mathrm{max}}^3 - 3R_{\mathrm{max}}^2 + 1}\right) \frac{\left(1 + \rho_{\mathrm{sp,m},i}R_{\mathrm{min}}\right)^2}{-C_{\mathrm{int},i}} \Delta \rho_{\mathrm{sp}}.\tag{C.3}$$

The cumulative melting time $\tau_{\mathrm{sp},i}$ is acquired from explicit forward time marching

$$\tau_{\mathrm{sp},i} = \tau_{\mathrm{sp},i-1} + \Delta \tau_{\mathrm{sp},i},\tag{C.4}$$

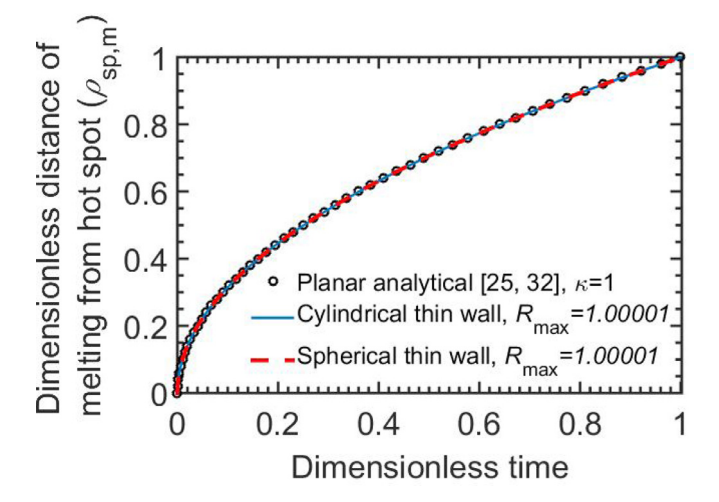


Fig. C1. Numerically calculated dimensionless melting distance for thin walled cylindrical and spherical geometries, agree with those using analytical solutions [26,33].

where $\tau_{\mathrm{sp},i=1}=0$ represents the initial condition. The reciprocal of $\tau_{\mathrm{sp},i=N+1}$ is the enhancement ratio, ϵ_{sp} .

As shown in Fig. C.1, the dimensionless melt distances using this numerical scheme for thin walls (i.e., $R_{\text{max}} = 1.00001$) agree with those determined using the analytical solution for the planar case [26,33]. This agreement validates the numerical scheme.

Appendix D. Derivation of the coefficients $C_{cv,i}$ in Eq. (9)

From Eq. (3), the volume fraction of metal mesh in $\kappa(\rho_{\rm sp})$ is $v_{\rm Mesh}(\rho_{\rm sp}) = [\kappa(\rho_{\rm sp})k_{\rm UE}-k_{\rm PCM}]/\Delta k$, where $\Delta k = k_{\rm Mesh}-k_{\rm PCM}$. By utilizing $\Delta r = r_{\rm o}-r_{\rm i}$, $r=r_{\rm i}+\Delta r\cdot\rho_{\rm sp}$ and $dr=\Delta r\cdot d\rho_{\rm sp}$ the conservation of metal volume fraction $\bar{v}_{\rm Mesh}=\left[\int_{r_{\rm i}}^{r_{\rm o}}dr~4\pi\,r^2~v_{\rm Mesh}(\rho_{\rm sp})\right]/[4\pi\,(r_{\rm o}^3-r_{\rm i}^3)/3]=v_{\rm UE}$ takes the form

$$\bar{\nu}_{\text{Mesh}} = \frac{3 \int_0^1 \Delta r d\rho_{\text{sp}} (r_{\text{i}} + \Delta r \rho_{\text{sp}})^2 \left[\kappa (\rho_{\text{sp}}) \frac{k_{\text{UE}}}{\Delta k} - \frac{k_{\text{PCM}}}{\Delta k} \right]}{(r_0^2 - r_0^2)}$$
(D.1)

For the uniformly enhanced case, $\kappa(\rho_{\rm sp}) = 1$ (i.e., $v_{\rm Mesh}(\rho_{\rm sp}) = [k_{\rm UE} - k_{\rm PCM}]/\Delta k$), and Eq. (D.1) becomes

$$\frac{3\int_0^1 \Delta r d\rho_{\rm sp}(r_{\rm i} + \Delta r \rho_{\rm sp})^2 \left[\frac{k_{\rm UE}}{\Delta k} - \frac{k_{\rm PCM}}{\Delta k}\right]}{(r_0^3 - r_{\rm i}^3)} = \frac{k_{\rm UE}}{\Delta k} - \frac{k_{\rm PCM}}{\Delta k}.$$
 (D.2)

Eq. (3) is substituted for $\kappa(\rho_{\rm sp})$ into Eq. (D.1), and after rearrangement

$$\frac{k_{\text{UE}}}{\Delta k} - \frac{k_{\text{PCM}}}{\Delta k} = \frac{3(R_{\text{max}} - 1)}{R_{\text{max}}^3 - 1} \left(\frac{k_{\text{UE}}}{\Delta k} \right) \\
\times \left\{ \sum_{i=0}^{i=n} \left[\frac{(R_{\text{max}} - 1)^2}{i+3} + \frac{2(R_{\text{max}} - 1)}{i+2} + \frac{1}{i+1} \right] C_i \right\} \\
- \frac{k_{\text{PCM}}}{\Delta k}.$$
(D.3)

Next $k_{\rm UE}/\Delta k$ and $k_{\rm PCM}/\Delta k$ in Eq. (D.3) are eliminated to yield,

$$1 = \frac{3(R_{\text{max}} - 1)}{R_{\text{max}}^3 - 1} \times \left\{ \sum_{i=0}^{i=n} \left[\frac{(R_{\text{max}} - 1)^2}{i+3} + \frac{2(R_{\text{max}} - 1)}{i+2} + \frac{1}{i+1} \right] C_i \right\}$$

$$= \sum_{i=n}^{i=n} C_{\text{cv},i} C_{i}.. \tag{D.4}$$

By comparison with Eq. (8) we find,

$$C_{\text{cv},i} = \left[\frac{(R_{\text{max}} - 1)^2}{i + 3} + \frac{2(R_{\text{max}} - 1)}{i + 2} + \frac{1}{i + 1} \right] \frac{3(R_{\text{max}} - 1)}{R_{\text{max}}^3 - 1}. \quad (D.5)$$

Appendix E. Equations and parameters in 1-D cylindrical coordinates

In 1-D cylindrical coordinates, the heat diffusion equation and energy balance at the melt-front take the form

$$\frac{1}{r}\frac{\partial}{\partial r}\left[rk(r)\frac{\partial T(r,t)}{\partial r}\right] = 0,$$
(E.1)

and

$$-k(r)\frac{\partial T(r,t)}{\partial r}\Big|_{r=r_{\rm m}(t)} = \lambda \frac{dr_{\rm m}(t)}{dt}.$$
 (E.2)

Eqs. (E.1) and (E.2) are nondimensionalized following Ref. [26] as

$$\frac{1}{(1+\rho R_{\min})} \frac{\partial}{\partial \rho} \left[(1+\rho R_{\min}) \kappa(\rho) \frac{\partial \theta(\rho, \tau_{r})}{\partial \rho} \right] = 0, \tag{E.3}$$

and

$$-\kappa(\rho) \frac{\partial \theta(\rho, \tau_{r})}{\partial \rho} \bigg|_{\rho = \rho_{m}(\tau_{r})} = \left(\frac{(R_{max} - 1)^{2}}{\frac{R_{max}^{2}}{2} \ln(R_{max}) - \frac{R_{max}^{2}}{4} + \frac{1}{4}} \right) \frac{d\rho_{m}(\tau_{r})}{d\tau_{r}}.$$
(E.4)

The enhancement ratio ($\epsilon_r=1/\tau_{r,max}$, where the subscript r represents 1-D cylindrical coordinates) is numerically determined using Eqs. (E.3) and (E.4) based on the procedures in Appendix C and Eq. (6).

From Eq. (3), the volume fraction of metal mesh in $\kappa(\rho)$ is $v_{\mathrm{Mesh}}(\rho) = [\kappa(\rho)k_{\mathrm{UE}} - k_{\mathrm{PCM}}]/\Delta k$, where $\Delta k = k_{\mathrm{Mesh}} - k_{\mathrm{PCM}}$. By utilizing $\Delta r = r_0 - r_{\mathrm{i}}$, $r = r_{\mathrm{i}} + \Delta r \cdot \rho$ and $dr = \Delta r \cdot d\rho$, the conservation of metal volume fraction for a cylinder $\bar{v}_{\mathrm{Mesh}} = \int_{r_{\mathrm{i}}}^{r_0} dr \ 2\pi r \ v_{\mathrm{Mesh}}(\rho) \bigg]/[\pi \ (r_0^2 - r_{\mathrm{i}}^2)] = v_{\mathrm{UE}}$ takes the form

$$\bar{v}_{\text{Mesh}} = \frac{2\int_0^1 \Delta r d\rho (r_i + \Delta r \rho) \left[\kappa(\rho) \frac{k_{\text{UE}}}{\Delta k} - \frac{k_{\text{PCM}}}{\Delta k}\right]}{(r_0^2 - r_i^2)}.$$
 (E.5)

For the uniformly enhanced case, $\kappa(\rho) = 1$ (i.e., $v_{\text{Mesh}}(\rho) = [k_{\text{UE}} - k_{\text{PCM}}]/\Delta k)$, and Eq. (E.5) becomes

$$\frac{2\int_0^1 \Delta r d\rho (r_i + \Delta r \rho) \left[\frac{k_{\text{UE}}}{\Delta k} - \frac{k_{\text{PCM}}}{\Delta k}\right]}{(r_0^2 - r_i^2)} = \frac{k_{\text{UE}}}{\Delta k} - \frac{k_{\text{PCM}}}{\Delta k}.$$
 (E.6)

Eq. (3) is substituted for $\kappa(\rho)$ in Eq. (E.5), and the equation is then rearranged as

$$\frac{k_{\text{UE}}}{\Delta k} - \frac{k_{\text{PCM}}}{\Delta k} = \frac{2(R_{\text{max}} - 1)}{R_{\text{max}}^2 - 1} \left(\frac{k_{\text{UE}}}{\Delta k}\right) \times \left\{\sum_{i=0}^{i=n} \left[\frac{(R_{\text{max}} - 1)}{i+2} + \frac{1}{i+1}\right] C_i\right\} - \frac{k_{\text{PCM}}}{\Delta k}.$$
(E.7)

Next $k_{\rm UE}/\Delta k$ and $k_{\rm PCM}/\Delta k$ in Eq. (E.7) are eliminated to yield,

$$1 = \frac{2(R_{\text{max}} - 1)}{R_{\text{max}}^2 - 1} \times \left\{ \sum_{i=0}^{i=n} \left[\frac{(R_{\text{max}} - 1)}{i+2} + \frac{1}{i+1} \right] C_i \right\}.$$
 (E.8)

By comparison with Eq. (8).

$$C_{\text{cv},i} = \left\lceil \frac{(R_{\text{max}} - 1)}{i + 2} + \frac{1}{i + 1} \right\rceil \frac{2(R_{\text{max}} - 1)}{R_{\text{max}}^2 - 1}.$$
 (E.9)

Eq. (E.9) is similar to the form in Eq. (D.5) for spherical systems.

For concave-up distributions specified by Eq. (10), $\Delta \kappa$ for 1-D cylindrical coordinates is obtained using the conservation of metal volume fraction $\bar{v}_{\text{Mesh}} = \left[\int_{r_{\rm i}}^{r_{\rm o}} dr \; 2\pi r \; v_{\text{Mesh}}(\rho)\right] / [\pi \, (r_{\rm o}^2 - r_{\rm i}^2)] = v_{\rm UE}$ as

$$\Delta \kappa = \frac{1 - \kappa_{\min}}{\frac{2(R_{\max} - 1)}{R_{\max} - \frac{2}{1}} \left(\frac{R_{\max}}{n+1} - \frac{R_{\min}}{n+2}\right)}.$$
 (E.10)

Appendix F. Derivation of the solution to constant power heat source cases

For the constant heat source with power q located at $r = r_i$ the Fourier Law applied at the meltfront takes the form,

$$q = 4\pi r^2 \left[-k(r) \frac{\partial T(r,t)}{\partial r} \right] \Big|_{r=r_{\rm m}(t)}. \tag{F.1}$$

For the case of UE with $k(r)=k_{\rm UE}, \ {\rm Eq.}\ ({\rm F.1})$ can be rearranged and integrated as

$$T_{\rm s}(t) = T_{\rm m} + \frac{q}{4\pi k_{\rm UE}} \left[\frac{1}{r_{\rm i}} - \frac{1}{r_{\rm m}(t)} \right].$$
 (F.2)

Then, the temperature $T_s(t)$ at heat source $(r = r_i)$ in Eq. (F.2) increases until the melt front reaches r_0 (i.e., $r_{m(t)} = r_0$).

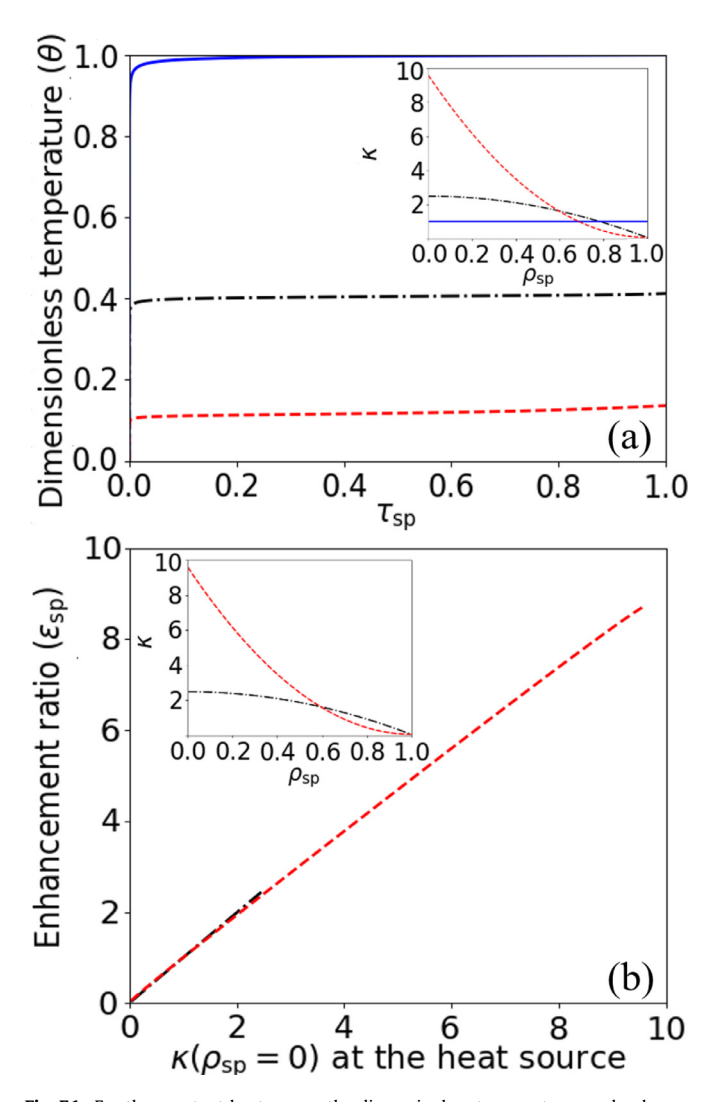


Fig. F.1. For the constant heat source the dimensionless temperatures and enhancement ratios are compared using $R_{\text{max}} = 101$. (a) The dimensionless temperature θ at $\tau_{\text{sp}} = 1$ using concave-up $\kappa\left(\rho_{\text{sp}} = 0\right)$ is lower than that of concave-down and $\kappa = 1$. (b) The enhancement ratio ($\epsilon = 8.7$) to the average temperature rise for the concave-up $\kappa(\rho_{\text{sp}})$ outperforms that ($\epsilon = 2.5$) of concave-down $\kappa(\rho_{\text{sp}})$.

To determine the melting time, the energy balance at the melt front is

$$q = 4\pi r^2 \lambda \left[\frac{dr_{\rm m}(t)}{dt} \right] \Big|_{r=r_{\rm m}(t)}, \tag{F.3}$$

and the melting time is determined by integration to be

$$t = \frac{4\pi\lambda(r_{\rm m}^3 - r_{\rm i}^3)}{3q},\tag{F.4}$$

which reaches a maximum $t_{\rm max}$ when $r_{\rm m}=r_{\rm o}$. Using $\rho_{\rm sp}=(r-r_{\rm i})/(r_{\rm o}-r_{\rm i})$, $\rho_{\rm sp,m}=(r_{\rm m}-r_{\rm i})/(r_{\rm o}-r_{\rm i})$, $\theta=[T_{\rm s}(t)-T_{\rm m}]/(T_{\rm s,UE}-T_{\rm m})$, and $\tau_{\rm sp}=t/t_{\rm max}$, the melting temperature in Eq. (F.2) and melting time in Eq. (F.4) can be nondimensionalized as

$$\theta = \frac{R_{\text{max}}\rho_{\text{sp,m}}}{1 + R_{\text{min}}\rho_{\text{sp,m}}},\tag{F.5}$$

and

$$\tau_{\rm sp} = \frac{(1 + R_{\rm min} \rho_{\rm sp,m})^3 - 1}{R_{\rm max}^3 - 1}.$$
 (F.6)

For k=k(r) the case of SE with $\kappa=k(r)/k_{\rm UE},$ Eq. (F.1) can be nondimensionalized as

$$-\kappa(\rho_{\rm sp})\frac{\partial \theta}{\partial \rho_{\rm sp}} = \frac{1}{\left[\frac{1}{R_{\rm max}} + 2\rho_{\rm sp}\frac{R_{\rm min}}{R_{\rm max}} + \rho_{\rm sp}^2\frac{R_{\rm min}^2}{R_{\rm max}}\right]_{\rho_{\rm sp}=\rho_{\rm sp,m}}}.$$
 (F.7)

Since there is no analytical solution for complex $\kappa(\rho_{\rm Sp})$, the dimensionless temperature θ must be determined by numerical integration as

$$\Delta\theta_{j} \approx -\frac{\Delta\rho_{\rm sp}}{\kappa \left(\rho_{\rm sp,j}\right) \left[\frac{1}{R_{\rm max}} + 2\rho_{\rm sp,j} \frac{R_{\rm min}}{R_{\rm max}} + \rho_{\rm sp,j}^{2} \frac{R_{\rm min}^{2}}{R_{\rm max}^{2}}\right]},\tag{F.8}$$

and the cumulative temperature θ_j is acquired from explicit forward marching

$$\theta_j = \theta_{j-1} + \Delta \theta_j, \tag{F.9}$$

$$\rho_{\text{sp},j} = \rho_{\text{sp},j-1} + \Delta \rho_{\text{sp}}, \tag{F.10}$$

where $\Delta \rho_{\rm sp} = 1/N$, and $\rho_{{\rm sp},j=1} = 0$ represent the initial condition for j >= 1.

The dimensionless temperature θ is shown as a function of τ_{sp} in Fig. F.1 (a). For all times, the concave up κ distribution minimizes θ . This result physically implies that PCM/mesh composites of higher κ at $\rho_{sp}=0$ are able to maintain the hot-spot at the lowest temperature.

For the constant heat source, the enhancement ratio is defined as $\epsilon = \overline{\theta_{\rm UE}}/\overline{\theta_{\rm SE}}$, which is the ratio of the average θ of UE to SE meshes. Ratios greater than one indicate that SE meshes maintain lower average temperature rises than UE meshes. As shown in Fig. F.1(b), the enhancement ratio ($\epsilon = 8.7$) for the concave-up $\kappa(\rho_{\rm sp})$ is higher than of concave $\kappa(\rho_{\rm sp})$ ($\epsilon = 2.5$). The enhancement ratio of $\epsilon = 8.7$ for constant hot-spot power is the same as the ϵ for heat dissipation with constant temperature (red line). The profiles of the enhancement ratio for various κ at $\rho_{\rm sp} = 0$ are identical to those of Fig. 4, where the heat source is at a constant temperature.

Supplementary material

Supplementary material associated with this article can be found, in the online version, at 10.1016/j.ijheatmasstransfer.2019. 119153

References

- N. KEDEM, Six things to know about smartphone batteries, (https://www.cnet. com/news/six-things-to-know-about-smartphone-batteries/). (accessed: January 28, 2018), 2012
- [2] P. Wang, A. Bar-Cohen, B. Yang, G.L. Solbrekken, A. Shakouri, Analytical modeling of silicon thermoelectric microcooler, J. Appl. Phys. 100 (1) (2006) 014501.
- [3] M. Hodes, R.D. Weinstein, S.J. Pence, J.M. Piccini, L. Manzione, C. Chen, Transient thermal management of a handset using phase change material (PCM), J. Electron. Packag. 124 (4) (2002) 419–426, doi:10.1115/1.1523061.
- [4] S.V. Garimella, Advances in mesoscale thermal management technologies for microelectronics, Microelectron. J. 37 (11) (2006) 1165–1185.
- [5] S. Krishnan, S.V. Garimella, G.M. Chrysler, R.V. Mahajan, Towards a thermal Moore's law, IEEE Trans. Adv. Packag. 30 (3) (2007) 462–474.
- [6] S.S. Anandan, V. Ramalingam, Thermal management of electronics: a review of literature, Therm. Sci. 12 (2) (2008) 5–26.
 [7] S. Krishnan, S.V. Garimella, Analysis of a phase change energy storage sys-
- [7] S. Krishnan, S.V. Garimella, Analysis of a phase change energy storage system for pulsed power dissipation, IEEE Trans. Compon. Packag. Technol. 27 (1) (2004) 191–199.
- [8] R. Chein, G. Huang, Thermoelectric cooler application in electronic cooling, Appl. Therm. Eng. 24 (14–15) (2004) 2207–2217.
- [9] C.J. Ho, L.C. Wei, Z.W. Li, An experimental investigation of forced convective cooling performance of a microchannel heat sink with al203/water nanofluid, Appl. Therm. Eng. 30 (2–3) (2010) 96–103.
- [10] T. Yousefi, S.A. Mousavi, B. Farahbakhsh, M.Z. Saghir, Experimental investigation on the performance of cpu coolers: effect of heat pipe inclination angle and the use of nanofluids, Microelectron. Reliab. 53 (12) (2013) 1954–1961.
- [11] S. Krishnan, S.V. Garimella, S.S. Kang, A novel hybrid heat sink using phase change materials for transient thermal management of electronics, IEEE Trans. Compon. Packag. Technol. 28 (2) (2005) 281–289.

- [12] N.S. Dhaidan, J. Khodadadi, Improved performance of latent heat energy storage systems utilizing high thermal conductivity fins: a review, J. Renew. Sustain. Energy 9 (3) (2017) 034103.
- [13] A. Elgafy, K. Lafdi, Effect of carbon nanofiber additives on thermal behavior of phase change materials, Carbon 43 (15) (2005) 3067–3074.
- [14] H. Huang, C. Liu, Y. Wu, S. Fan, Aligned carbon nanotube composite films for thermal management, Adv. Mater. 17 (13) (2005) 1652–1656.
- [15] S. Kim, L.T. Drzal, High latent heat storage and high thermal conductive phase change materials using exfoliated graphite nanoplatelets, Solar Energy Mater. Solar Cells 93 (1) (2009) 136–142.
- [16] F. Yavari, H.R. Fard, K. Pashayi, M.A. Rafiee, A. Zamiri, Z. Yu, R. Ozisik, T. Borca-Tasciuc, N. Koratkar, Enhanced thermal conductivity in a nanostructured phase change composite due to low concentration graphene additives, J. Phys. Chem. C 115 (17) (2011) 8753–8758.
- [17] S.N. Schiffres, S. Harish, S. Maruyama, J. Shiomi, J.A. Malen, Tunable electrical and thermal transport in ice-templated multilayer graphene nanocomposites through freezing rate control, ACS Nano 7 (12) (2013) 11183–11189.
- [18] H. Ji, D.P. Sellan, M.T. Pettes, X. Kong, J. Ji, L. Shi, R.S. Ruoff, Enhanced thermal conductivity of phase change materials with ultrathin-graphite foams for thermal energy storage, Energy Environ. Sci. 7 (3) (2014) 1185– 1192.
- [19] G.E.I. Humphries W. R., A design handbook for phase change thermal control and energy storage devices, NASA Technical paper, 1977.
- [20] K. Lafdi, O. Mesalhy, S. Shaikh, Experimental study on the influence of foam porosity and pore size on the melting of phase change materials, J. Appl. Phys. 102 (8) (2007) 083549.
- [21] L. Fan, J.M. Khodadadi, Thermal conductivity enhancement of phase change materials for thermal energy storage: a review, Renew. Sustain. Energy Rev. 15 (1) (2011) 24–46.
- [22] H. Wang, F. Wang, Z. Li, Y. Tang, B. Yu, W. Yuan, Experimental investigation on the thermal performance of a heat sink filled with porous metal fiber sintered felt/paraffin composite phase change material, Appl. Energy 176 (2016) 221–232.
- [23] J.P. Kruth, M.C. Leu, T. Nakagawa, Progress in additive manufacturing and rapid prototyping, CIRP Ann. - Manuf. Technol. 47 (2) (1998) 525–540.
- [24] I. Gibson, D.W. Rosen, B. Stucker, Additive Manufacturing Technologies, 238, Springer, 2010.
- [25] W.E. King, A.T. Anderson, R.M. Ferencz, N.E. Hodge, C. Kamath, S.A. Khairallah, A.M. Rubenchik, Laser powder bed fusion additive manufacturing of metals; physics, computational, and materials challenges, Appl. Phys. Rev. 2 (4) (2015) 041304
- [26] L.C. Wei, J.A. Malen, Amplified charge and discharge rates in phase change materials for energy storage using spatially-enhanced thermal conductivity, Appl. Energy 181 (2016) 224–231.
- [27] C. Rogers, On a class of moving boundary problems in non-linear heat conduction: application of a Bcklund transformation, Int. J. Nonlinear Mech. 21 (4) (1986) 249–256.
- [28] C. Rogers, P. Broadbridge, On a nonlinear moving boundary problem with heterogeneity: application of a reciprocal transformation, Z. Angew. Math. Phys. ZAMP 39 (1) (1988) 122–128.
- [29] B. Šarler, Stefan's work on solid-liquid phase changes, Eng. Anal. Bound. Elem. 16 (2) (1995) 83–92.
- [30] M.F. Natale, D.A. Tarzia, Explicit solutions to the one-phase Stefan problem with temperature-dependent thermal conductivity and a convective term, Int. J. Eng. Sci. 41 (15) (2003) 1685–1698.
- [31] L. Jiji, Heat Conduction, Springer Berlin Heidelberg, 2009.
- [32] D. Tarzia, Explicit and approximated solutions for heat and mass transfer problems with a moving interface, Advanced Topics in Mass Transfer, InTech, 2011.
- [33] V.R. Voller, F. Falcini, Two exact solutions of a Stefan problem with varying diffusivity, Int. J. Heat Mass Transf. 58 (1–2) (2013) 80–85.
- [34] B. Gowreesunker, S. Tassou, M. Kolokotroni, Improved simulation of phase change processes in applications where conduction is the dominant heat transfer mode, Energy Build. 47 (2012) 353–359.
- [35] M.S. Al-Jethelah, S.H. Tasnim, S. Mahmud, A. Dutta, Melting of nano-phase change material inside a porous enclosure, Int. J. Heat Mass Transf. 102 (2016) 773–787.
- [36] A. Bejan, Theory of melting with natural convection in an enclosed porous medium, J. Heat Transf. 111 (2) (1989) 407–415.
- [37] S. Krishnan, J.Y. Murthy, S.V. Garimella, Analysis of solid-liquid phase change under pulsed heating, J. Heat Transf. 129 (3) (2007) 395–400.
- [38] P.M. Teertstra, M.M. Yovanovich, J.R. Culham, Natural convection measurements for a concentric spherical enclosure, J. Heat Transf. 128 (6) (2006) 580– 587.
- [39] D. Nield, Effects of local thermal nonequilibrium in steady convective processes in a saturated porous medium: forced convection in a channel, J. Porous Media 1 (1998) 181–186.
- [40] W. Minkowycz, A. Haji-Sheikh, K. Vafai, On departure from local thermal equilibrium in porous media due to a rapidly changing heat source: the sparrow number, Int. J. Heat Mass Transf. 42 (18) (1999) 3373–3385.
- [41] O. Mesalhy, K. Lafdi, A. Elgafy, K. Bowman, Numerical study for enhancing the thermal conductivity of phase change material (PCM) storage using high thermal conductivity porous matrix, Energy Convers. Manag. 46 (6) (2005) 847–867
- [42] S. Whitaker, The Method of Volume Averaging, 13, Springer Science & Business Media, 2013.

- [43] T. Bergman, F. Incropera, A. Lavine, Fundamentals of Heat and Mass Transfer,
- Wiley, 2011.
 [44] F. Agyenim, N. Hewitt, P. Eames, M. Smyth, A review of materials, heat transfer and phase change problem formulation for latent heat thermal energy storage systems (LHTESS), Renew. Sustain. Energy Rev. 14 (2) (2010) 615–628.
 [45] J. Wang, J.K. Carson, M.F. North, D.J. Cleland, A new approach to modelling the effective thermal conductivity of heterogeneous materials, Int. J. Heat Mass
- Transf. 49 (17–18) (2006) 3075–3083.
- [46] D. Caudwell, J. Trusler, V. Vesovic, W. Wakeham, The viscosity and density of n-dodecane and n-octadecane at pressures up to 200 MPa and temperatures up to 473 K, Int. J. Thermophys. 25 (5) (2004) 1339–1352.

 [47] engineeringtoolbox, Volumetric coefficient of expansion, (https://www.engineeringtoolbox.com/cubical-expansion-coefficients-d_1262.html). (ac-
- cessed: September 10, 2018).
- [48] wolframalpha, chemical+n-octadecane, (http://www.wolframalpha.com/input/?i=chemical+N-octadecane). (accessed: September 10, 2018).